

¹ Study of the multi-strange resonance $\Xi(1530)^0$ production
² with ALICE at the LHC energies

³ Jihye Song

4 Contents

5	List of Figures	4
6	List of Tables	6
7	1 The physics of relativistic heavy-ion collisions	7
8	1.1 Standard model	7
9	1.2 Quantum Chromo-Dynamics	7
10	1.3 Heavy Ion Collisions	7
11	2 Production of resonance with strangeness	7
12	2.1 Resonance with strangeness	7
13	3 Theoretical models	7
14	3.1 Thermal statistical model	7
15	3.1.1 Calculations	9
16	3.1.2 Results	9
17	3.1.3 Comparison with data	11
18	3.2 UrQMD	11
19	4 A Large Ion Collider Experiment at the LHC	11
20	4.1 The Large Hadron Collider	12
21	4.2 The ALICE project	12
22	4.2.1 ALICE detector	12
23	4.2.2 Data Acquisition (DAQ) and trigger system	12
24	4.2.3 ALICE offline software frame work	12
25	5 Measurement of $\Xi(1530)^0$ production in p-Pb and Pb-Pb	12
26	5.1 $\Xi(1530)^0$ -reconstruction	13
27	5.1.1 Data sample and event selection	13
28	5.1.2 Track and topological selection	16
29	5.1.3 Particle identification	19
30	5.1.4 Signal extraction	21
31	5.2 Efficiency correction	29
32	5.3 Corrected p_T -spectra	32
33	5.4 Systematic uncertainties	34
34	5.5 $\Xi(1530)^0$ transverse momentum spectra	39
35	6 Results	42
36	6.1 dN/dy and $\langle p_T \rangle$	42
37	6.2 Particle yield ratios	42

38	6.2.1	Comparison with other resonances	42
39	6.2.2	Comparison with models	42
40	References		42

41 **List of Figures**

42 1	Ratio of baryonic and mesonic resonances over their stable partner as a function of temperature.	10
44 2	Ratio of resonances over their stable partner as a function of $\sqrt{(s)}$	11
45 3	Vertex-z coordinate distribution of the accepted events in p–Pb collision(Left) and in Pb–Pb collisions(Right). The red dashed line indicates vertex cut	14
47 4	Multiplicity distribution of accepted events in p–Pb collision in percentile. The each color and labels define the four intervals in which the analysis is performed.	15
50 5	Centrality distribution of three different trigger classes.	16
51 6	Sketch of the decay modes for Ξ^{*0} (right) and depiction of the track and topological selection criteria.	18
53 7	TPC dE/dx as function of transverse momentum for total (top) and selected first emitted π in 3σ (bottom)	19
55 8	TPC dE/dx as function of transverse momentum for total (top) and selected second emitted π in 3σ (bottom)	19
57 9	TPC dE/dx as function of transverse momentum for total (top) and selected last emitted π in 3σ (bottom)	20
59 10	TPC dE/dx as function of transverse momentum for total (top) and selected proton in 3σ (bottom)	20
61 11	The $\Xi^\mp\pi^\pm$ invariant mass distribution (Same-event pairs) in $1.8 < p_T < 2.2 \text{ GeV}/c$ and for the multiplicity class 20-40%. The background shape, using pairs from different events (Mixed-event background), is normalised to the counts in $1.49 < M_{\Xi\pi} < 1.51 \text{ GeV}/c^2$ and $1.56 < M_{\Xi\pi} < 1.58 \text{ GeV}/c^2$	21
65 12	The $\Xi^\mp\pi^\pm$ invariant mass distribution (Same-event pairs) in $3.0 < p_T < 3.5 \text{ GeV}/c$ and for the centrality class 0-10%. The background shape, using pairs from different events (Mixed-event background), is normalised to the counts in $1.49 < M_{\Xi\pi} < 1.51 \text{ GeV}/c^2$ and $1.56 < M_{\Xi\pi} < 1.58 \text{ GeV}/c^2$	22
69 13	The invariant mass distribution after subtraction of the mixed-event background in p–Pb collisions. The solid curve represents the combined fit, while the dashed line describes the residual background.	23
72 14	The invariant mass distribution after subtraction of the mixed-event background in Pb–Pb collisions. The solid curve represents the combined fit, while the dashed line describes the residual background.	24
75 15	σ fit parameters as a function of p_T in MB in p–Pb collisions (top) and in Pb–Pb collisions (bottom).	26
77 16	$\Xi(1530)^0$ -mass obtained from fit of the Voigtian peak as a function of p_T in each multiplicity classes in p–Pb collisions (top) and the different centrality classes in Pb–Pb (bottom).	27

80	17	$\Xi(1530)^0$ -raw spectra obtained from fit of the Voigtian peak and a polynomial residual background for different multiplicities in p–Pb collisions (top) and Pb–Pb collisions (bottom). Only the statistical error is reported.	28
81			
82	18	$\Xi(1530)^0$ -raw spectra obtained from fit of the Voigtian peak and a polynomial residual background for different multiplicities. Only the statistical error is reported.	29
83			
84	19	Real corrected $\Xi(1530)^0$ spectrum (black) for the minimum bias with Levy fit (black curve). Also shown are the unweighted generated (blue) and reconstructed (red) $\Xi(1530)^0$ spectra.	30
85			
86	20	Efficiency as a function of p_T in minimum bias events in p–Pb collisions. . .	31
87			
88	21	Efficiency as a function of p_T in different centrality classes in Pb–Pb collisions	32
89			
90	22	Corrected p_T -spectra of $\Xi(1530)^0$ in NSD and different multiplicity classes in p–Pb collisions.	33
91			
92	23	Corrected p_T -spectra of $\Xi(1530)^0$ in different centrality classes in Pb–Pb collisions.	33
93			
94	24	Summary of the contributions to the systematic uncertainty in minimum bias events in p–Pb collisions. The dashed black line is the sum in quadrature of all the contributions.	37
95			
96	25	Systematic uncertainties for each multiplicity classes in p–Pb collisions. . .	37
97			
98	26	Summary of the contributions to the systematic uncertainty in minimum bias events in Pb–Pb collisions. The dashed black line is the sum in quadrature of all the contributions.	38
99			
100	27	Systematic uncertainties for each multiplicity classes.	38
101			
102	28	Corrected yields as function of p_T in NSD events and multiplicity dependent event classes in p–Pb collision system. Statistical uncertainties are presented as bar and systematical uncertainties are plotted as boxes.	40
103			
104	29	Corrected yields as function of p_T in different centrality classes in Pb–Pb collision system. Statistical uncertainties are presented as bar and systematical uncertainties are plotted as boxes.	41
105			
106			
107			
108			

¹⁰⁹ **List of Tables**

110	1	Parameters used in the thermal-model calculations.	8
111	2	Properties of particles used in the ratio calculations.	9
112	3	Difference of mass (ΔM), baryon number (ΔB), strangeness (ΔS) and charge (ΔQ) of the ratios. The values of the slopes needs to be checked!!!! .	11
113	4	Number of accepted and analysed events per multicity interval	16
114	5	Track selections common to all decay daughters and primary track selections applied to the charged pions from decays of Ξ^{*0}	17
115	6	Topological and track selection criteria.	17
116	7	Summary of the systematic uncertainties on the differential yield, $d^2N/(dp_T dy)$. Minimum and maximum values in all p_T intervals and multiplicity classes in p–Pb, centrality classes in Pb–Pb are shown for each source.	39
117			
118			
119			
120			

121 **1 The physics of relativistic heavy-ion collisions**

122 This test for references [1]

123 **1.1 Standard model**

124 **1.2 Quantum Chromo-Dynamics**

125 **1.3 Heavy Ion Collisions**

126 **2 Production of resonance with strangeness**

127 **2.1 Resonance with strangeness**

128 **3 Theoretical models**

129 **3.1 Thermal statistical model**

130 The statistical-thermal model has proved extremely successful in applications to relativistic
131 collisions of both heavy ions and elementary particles. In light of this success, THERMUS,
132 a thermal model analysis package, has been developed for incorporation into the object-
133 oriented ROOT framework [2].

134 There are three types of statistical-thermal models in explaining data in high energy nu-
135 clear physics and THERMUS treats the system quantum numbers B (baryon number), S
136 (strangeness) and Q (charge) within three distinct formalisms:

138 1. **Grand-Canonical Ensemble:** Because the hot dense matter produced in nucleus-
139 nucleus collisions is large enough, this ensemble is the most widely used in applications
140 to heavy-ion collisions, in which the quantum numbers are conserved on average.

141 2. **Fully-Canonical Ensemble:** In which B, S and Q are each exactly conserved and
142 this ensemble used in high-energy elementary collisions such as pp, p \bar{p} and e $^-$ e $^+$
143 collisions.

144 3. **Strangeness-Canonical Ensemble:** In small systems or at low temperatures, a
145 canonical treatment leads to a suppression of hadrons carrying non-zero quantum
146 numbers, since these particles have to be created in pairs and the resulting low
147 production of strange particles requires a canonical treatment of strangeness.

148 In order to calculate the thermal properties of a system, one starts with an evaluation
149 of its partition function. The form of the partition function obviously depends on the
150 choice of ensemble. In the present analysis the strangeness-canonical ensemble used and
151 the statistical-thermal model requires six parameters as input: the chemical freeze-out

152 temperature T , baryon and charge chemical potentials μ_B and μ_Q respectively, canonical
153 or correlation radius, R_C ; the radius inside which strangeness is exactly conserved and the
154 fireball radius R . An additional strangeness saturation factor γ_S has been used as indicator
155 of a possible departure from equilibrium and $\gamma_S = 1.0$ corresponds to complete strangeness
156 equilibration.

157 The volume dependence cancels out when studying the particle ratios as well as strangeness
158 canonical equivalent to grand canonical formalism if $\Delta S = 0$ in the ratios and γ_S also can-
159 cels out. Parameters used in the analysis listed in Table 1. The μ_B parameter taken from
160 the Ref. [3].

Table 1: Parameters used in the thermal-model calculations.

Parameter	Value
T (MeV)	varied (see text)
μ_B (MeV)	$9.2 \times 10^{-2}????$
μ_Q (MeV)	0.0
γ_S	1.0

161

162 **3.1.1 Calculations**

163 *Concept:*

164 In order to calculate the particle ratios within strangeness canonical formalism of THER-
 165 MUS, temperature varied between 60 MeV to 180 MeV and particle yields extracted for
 166 each temperature value and then primary particle ratios calculated for each case.

167

168 *Feed-Down Correction:*

169 Since the particle yields measured by the detectors in collision experiments include feed-
 170 down from heavier hadrons and hadronic resonances, the primordial hadrons are allowed to
 171 decay to particles considered stable by the experiment before model predictions are com-
 172 compared with experimental data. In the analysis only Λ particles counted as stable (do not
 173 allowed to decay) so there is no feed-down contribution from these particles to the other
 174 ratios.

175

176

177 Properties of studied particles and their particle ratios listed in Table 2 and Table 3,
 178 respectively.

Table 2: Properties of particles used in the ratio calculations.

Particle	Δ^{++}	p	K^{*0}	K^0	K^+	Λ^*	Λ	Σ^{*+}	Σ^+	Σ^0
Mass (MeV/c^2)	1232	938.27	895.92	497.61	493.67	1519.5	1115.68	1382.8	1189.37	1192.6
Width (MeV/c^2)	120	–	50.7	–	–	15.6	–	37.6	–	–
$c\tau$ (fm)	1.6	–	3.9	–	–	12.6	–	5.51	–	–
Ang. Momentum (J)	3/2	1/2	1	1	0	3/2	1/2	3/2	1/2	1/2
Isospin (I)	3/2	1/2	1/2	1/2	1/2	0	0	1	1	1
Parity (P)	+1	+1	-1	-1	0	-1	+1	+1	+1	+1
Strangeness (S)	0	0	1	1	1	-1	-1	-1	-1	-1
Baryon Number (B)	1	1	0	0	0	1	1	1	1	1
Decay Channel	$p\pi^+$	–	π^-	–	$\mu^+\nu_\mu$	pK^-	$p\pi^-$	$\Lambda\pi^+$	$p\pi^0$	$\Lambda\gamma$
Branching Ratio (%)	~ 100	–	~ 66.7	–	~ 63.54	~ 45	~ 63.9	~ 87	~ 51.6	~ 100
Q-Value(MeV/c^2)	154.16	–	262.68	–	–	87.55	37.84	127.55	111.53	76.96

179

180

181 **3.1.2 Results**

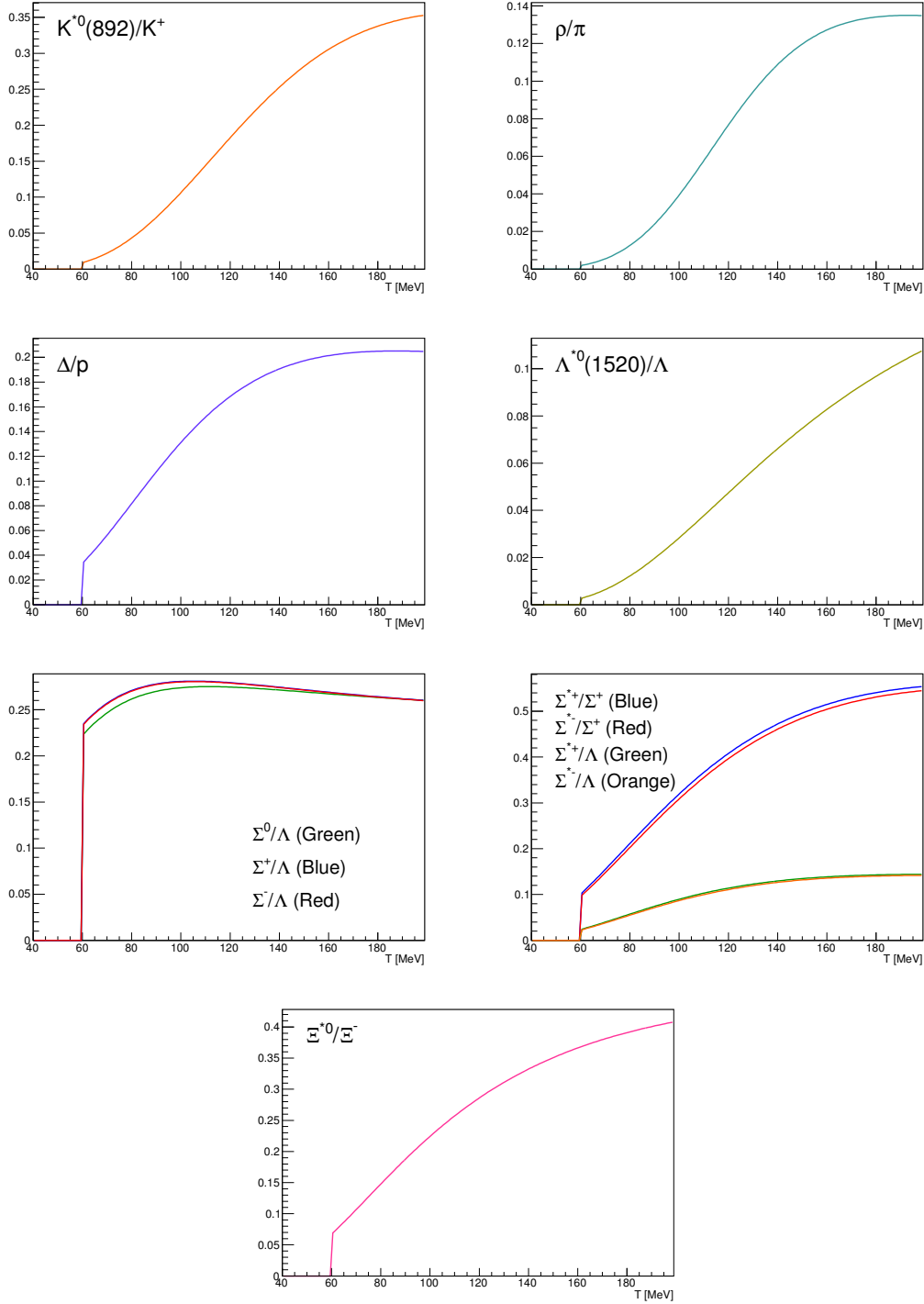


Figure 1: Ratio of baryonic and mesonic resonances over their stable partner as a function of temperature.

Table 3: Difference of mass (ΔM), baryon number (ΔB), strangeness (ΔS) and charge (ΔQ) of the ratios. The values of the slopes needs to be checked!!!!

Particle	Δ^{++}/p	K^*/K^+	Λ^*/Λ	Σ^{*+}/Λ	Σ^{*+}/Σ^0	Σ^0/Λ	Σ^{*+}/Σ^+	Ξ^{*0}/Ξ^-
ΔM (MeV/ c^2)	293.8	402.25	403.82	267.12	190.16	76.96	193.43	210.49
ΔB	0	0	0	0	0	0	0	0
ΔS	0	0	0	0	0	0	0	0
ΔQ	+1	-1	0	+1	0	+1	0	-1
Slope (%) per MeV ????????	0.19	0.76	0.98	0.25	-	-0.08	0.37	0.42

182 3.1.3 Comparison with data

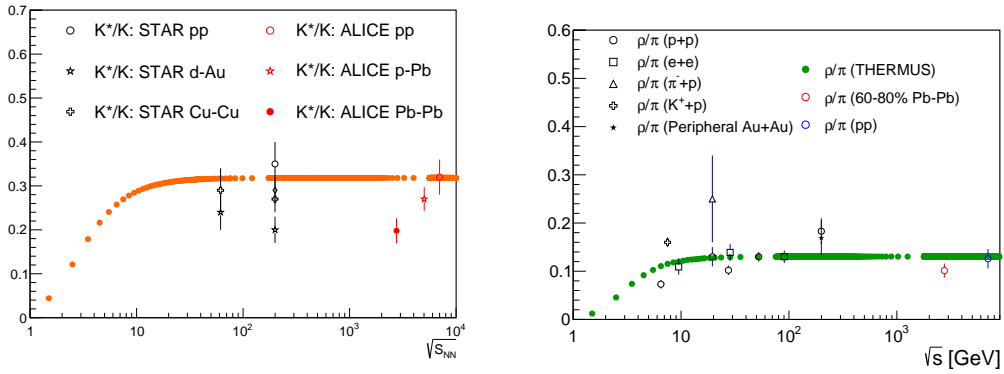


Figure 2: Ratio of resonances over their stable partner as a function of $\sqrt{(s)}$.

183 3.2 UrQMD

184 4 A Large Ion Collider Experiment at the LHC

185 ALICE (A Large Ion Collider Experiment) has been collecting data during the whole first
 186 phase of the Large Hadron Collider operations, from its startup on the 23 November 2009
 187 to the beginning of the first long technical shutdown in February 2013. During the first
 188 three years of operations LHC provided pp collisions at 0.9, 2.76, 7 and 8 TeV, Pb?Pb
 189 collisions at 2.76A TeV and finally p?Pb collisions at 5.02 TeV. The first section of this
 190 chapter focuses on the LHC performance during this phase and includes details on the
 191 accelerator parameters that allow the LHC to perform as a lead ion collider. A detailed
 192 description of the ALICE detector follows in the section 2.2. ALICE has been designed and

193 optimized to study the high particle-multiplicity environment of ultra-relativistic heavy-ion
194 collisions and its tracking and particle identification performance in Pb-Pb collisions are
195 discussed. The attention is drawn in particular on the central barrel detectors. Section
196 2.3 de- scribes the ALICE Data Acquisition (DAQ) system, that also embeds tools for the
197 online Data Quality Monitoring (DQM). The final part of the chapter is dedicated to the
198 offline computing and reconstruction system based on the GRID framework.

199 4.1 The Large Hadron Collider

200 The Large Hadron Collider (LHC) [57], [58] is a two-ring-superconducting hadron accel-
201 erator and collider installed in the 26.7 Km tunnel that hosted the LEP ma- chine and it
202 completes the CERN accelerator complex together with the PS and SPS, among the others
203 shown in fig. 2.1. Four main experiments are located in four different interaction points
204 along its circumference. ATLAS and CMS, the biggest ones, are multi-purpose detectors
205 built to discover the Higgs boson and hints of new physics beyond the Standard Model.
206 LHCb is dedicated to the physics of the flavour, focusing on the study CP-violation using B
207 meson decay channels. The phenomena that these three experiments aim to observe have
208 production cross sec- tion of the order of a hundred of pb or lower, therefore a large number
209 of collision events is required to the machine in order to fulfill the LHC pp physics program.
210 ALICE, on the contrary, is dedicated to the physics of Quark Gluon Plasma through the
211 observation of high-energy heavy-ion collisions, although a shorter physics pro- gram with
212 pp collisions has been carried out.

213 4.2 The ALICE project

214 4.2.1 ALICE detector

215 4.2.2 Data Acquisition (DAQ) and trigger system

216 4.2.3 ALICE offline software frame work

217 5 Measurement of $\Xi(1530)^0$ production in p–Pb and Pb–Pb

218 The measurement of resonance production in p–Pb collisions helps to disentangle cold
219 nuclear matter effects from genuine hot medium effects and contribute to the study of
220 the system size dependence of re-scattering in the hadronic phase. And the measurement
221 in ultra-relativistic heavy-ion collisions such as Pb–Pb collisions, provide information on
222 the properties of hadronic medium and different stage of its evolution. In order to study
223 the particle production mechanism in the hadronic phase between the chemical and ki-
224 netic freeze-out, the $\Xi(1530)^0$ resonance production at mid-rapidity($-0.5 < y_{\text{CMS}} < 0$) is
225 measured in p–Pb collisions $\sqrt{s_{\text{NN}}} = 5.02$ TeV and in Pb–Pb collisions with $|y| < 0.5$ at
226 $\sqrt{s_{\text{NN}}} = 2.76$ TeV with the ALICE experiment, via the reconstruction of its hadronic decay
227 into $\Xi\pi$.

228 **5.1 $\Xi(1530)^0$ -reconstruction**

229 The Ξ^{*0} production in p–Pb and Pb–Pb collisions at mid-rapidity has been studied in dif-
230 ferent multiplicity classes, from very central to peripheral collisions. The analysis strategy
231 is based on the invariant mass study of the reconstructed pairs (referred to as the candi-
232 dates) whose provenance could be the decay of a Ξ^{*0} baryon into charged particles. The
233 decay products (also called daughters in the text) are identified as oppositely charged Ξ and
234 π among the tracks reconstructed in the central barrel. The event selection, track selec-
235 tion and the particle identification strategy is described. The raw signal yield is extracted
236 by fitting the background-subtracted invariant mass distribution in several transverse mo-
237 mentum intervals. In order to extract the p_T -dependent cross section, these yields are
238 corrected for efficiency. The p_T -dependent correction due to the detector acceptance and
239 reconstruction efficiency, $(\text{Acc} \times \epsilon_{rec})(pt)$, is computed from a Monte Carlo simulation.
240 The absolute normalisation is then performed, by dividing for the number of the events in
241 each multiplicity and centrality classes.

242 **5.1.1 Data sample and event selection**

243 A description of the ALICE detector and of its performance during the LHC Run 1 (2010–
244 2013) can be found in [4, 5]. The data sample in the analysis from Pb–Pb collisions with
245 energy of $\sqrt{s_{\text{NN}}}=2.76$ obtained during 2011 and the sample of p–Pb run at $\sqrt{s_{\text{NN}}}=5.02$
246 TeV was recorded in 2013.

247 Due to the asymmetric energies of the proton (4 TeV) and lead ion (1.57 A TeV) beams,
248 the centre-of-mass system in the nucleon-nucleon frame is shifted in rapidity by $\Delta y_{\text{NN}} =$
249 0.465 towards the direction of the proton beam with respect to the laboratory frame of
250 the ALICE detector [6]. For the analysed p–Pb data set, the direction of the proton beam
251 was towards the ALICE muon spectrometer, the so-called “C” side, standing for negative
252 rapidities; conversely, the Pb beam circulated towards positive rapidities, labelled as “A”
253 side in the following. The analysis in this paper was carried out at midrapidity, in the
254 rapidity window $-0.5 < y_{\text{CMS}} < 0$.

255 The minimum-bias trigger during the p–Pb run was configured to select events by
256 requiring a logical OR of signals in V0A and V0C [5], two arrays of 32 scintillator detectors
257 covering the full azimuthal angle in the pseudo-rapidity regions $2.8 < \eta_{\text{lab}} < 5.1$ and
258 $-3.7 < \eta_{\text{lab}} < -1.7$, respectively [7]. In the data analysis it was required to have a
259 coincidence of signals in both V0A and V0C in order to reduce the contamination from
260 single-diffractive and electromagnetic interactions. Out of this sample in p–Pb collision
261 events about 109.3 million events, 93.9 million events satisfy the following selection criteria
262 and have been actually used for the analysis.

263 The Pb–Pb collisions data sample was selected by online centrality trigger requiring
264 a signal in the forward V0 detectors[8] to record enhanced data in central collision. The
265 data consists of 24.8 million events in most central collisions (0-10%), 21.8 million events in
266 semi-central collisions (10-50%) and 3.5 million events with minimum-bas trigger (0-90%).

267 Among 49.6 million events in total, 43.0 million events have been analyzed as passed the
 268 criteria below.

- 269 • Events with z-coordinate of primary vertex (V_z) falling within ± 10 cm from the
 270 interaction point
- 271 • Rejection of pile-up event
- 272 • Requiring primary tracks to have at least one hit in one of the two innermost layers
 273 of the ITS (silicon pixel detector, SPD)
- 274 • p–Pb: multiplicity ranges in percentile (V0A): 0-20%, 20-40%, 40-60%, 60-100% and
 275 MB(0-100%)
- 276 • Pb–Pb: centrality classes (V0A and V0C): 0-10%, 10-40%, 40-80% and MB (0-80%)

277 The distribution of the vertex z position of the accepted events in p–Pb collision is
 278 reported on left panel in Figure 3 and corresponding figure but obtained from Pb–Pb
 279 collisions is shown on right panel in Figure. 3. Events with $|V_z| < 10$ cm have been used
 280 to ensure a uniform acceptance in the central pseudo-rapidity region, $|\eta| < 0.8$, where the
 281 analysis is performed. This cut reduces the total number of events to 97.5 million events,
 282 that is the $\sim 89.2\%$ of the initial sample in p–Pb collisions and 43.04 million events which
 283 is $\sim 86.8\%$ of the initial sample in Pb–Pb collisions are survived.

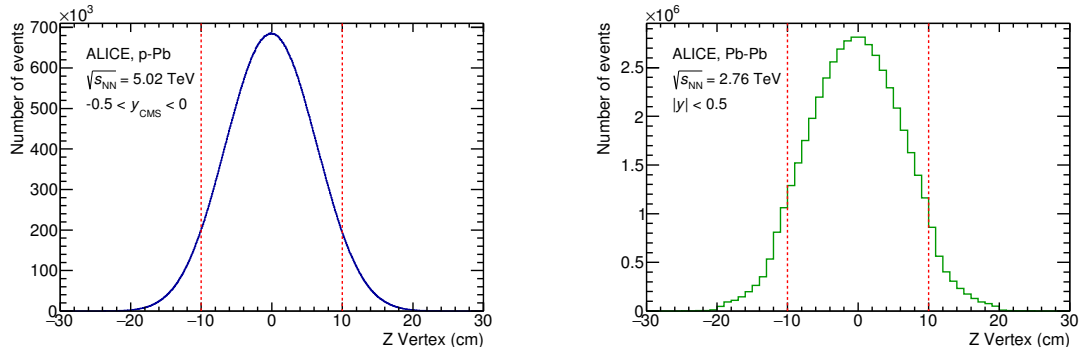


Figure 3: Vertex-z coordinate distribution of the accepted events in p–Pb collision(Left) and in Pb–Pb collisions(Right). The red dashed line indicates vertex cut

284 Fig. 4 shows the multiplicity distribution of the accepted events in p–Pb collision
 285 divided in bins of percentile. The each color on the histogram indicate the multiplicity
 286 ranges used in this analysis. Corresponding events for each multiplicity range are in Table
 287 4.

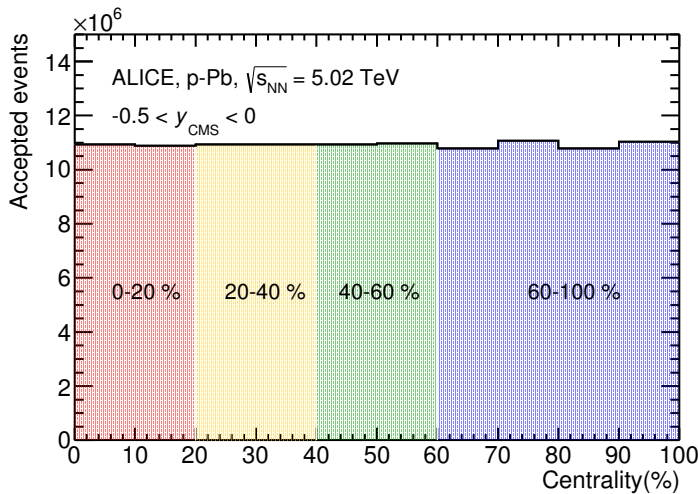


Figure 4: Multiplicity distribution of accepted events in p–Pb collision in percentile. The each color and labels define the four intervals in which the analysis is performed.

The distribution of centrality in each trigger used to select the events in Pb–Pb collision is shown in Fig. 5 and the reason why the centrality has step structure is that there are three different trigger classes classified by the amplitude threshold on VZERO detector. Because the distribution of events as function of centrality is not a flat, this may lead to additional bias, in particular when one needs to combine the results from different triggers. For example, events from 40-80% centrality bin have bias with high statistics in 40-60%. In order to avoid this effect, we have applied a flattening procedure to have flat distribution of events as function of centrality. A brief explanation of the method is below :

1. Histograms are obtained for the effective mass distribution in 1% centrality bins and for the centrality distribution
 2. The effective mass distributions are scaled in each 1% centrality bin by a factor:
Factor = Nevent in 20-40% / 20 / Nevent in current 1% bin
 3. Each bin in the centrality distribution is scaled using the factor described above
 4. Histograms are added for centrality bins of interest: 0-10%, 10-40%, 40-80%, 0-80%
- The resulting number of events in each centrality classes is summarized in Table 4.

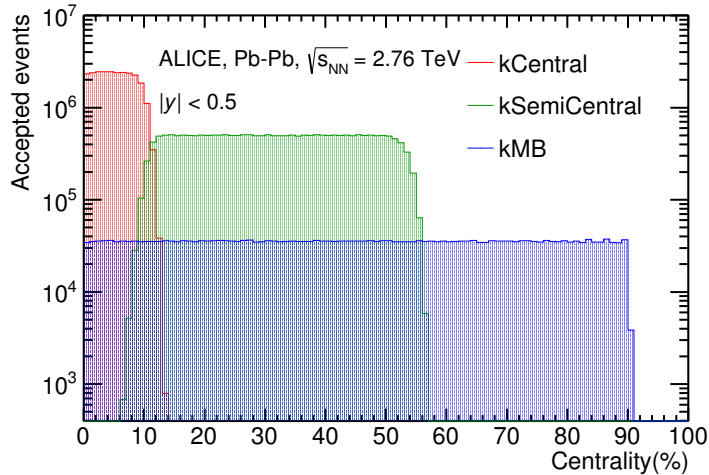


Figure 5: Centrality distribution of three different trigger classes.

p-Pb	0-20%	21.82×10^6
	20-40%	21.86×10^6
	40-60%	21.91×10^6
	60-100%	43.68×10^6
Pb-Pb	0-10%	5.58×10^6
	10-40%	16.73×10^6
	40-80%	22.31×10^6

Table 4: Number of accepted and analyzed events per multiplicity/centrality interval

303 5.1.2 Track and topological selection

304 In comparison with the Ξ^{*0} analysis carried out in pp collisions at $\sqrt{s} = 7$ TeV [9], track
 305 and topological selections were revised and adapted to the p-Pb dataset. Pions from strong
 306 decays of Ξ^{*0} were selected according to the criteria for primary tracks. As summarized
 307 in Table 5, all charged tracks were selected with $p_T > 0.15$ GeV/c and $|\eta_{\text{lab}}| < 0.8$, as
 308 described in Ref. [5]. The primary tracks were chosen with the Distance of Closest Approach
 309 (DCA) to PV of less than 2 cm along the longitudinal direction (DCA_z) and lower than $7\sigma_r$
 310 in the transverse plane (DCA_r), where σ_r is the resolution of DCA_r . The σ_r is strongly
 311 p_T -dependent and lower than 100 μm for $p_T > 0.5$ GeV/c [5]. To ensure a good track
 312 reconstruction quality, candidate tracks were required to have at least one hit in one of the
 313 two innermost layers (SPD) of the ITS and to have at least 70 reconstructed points in the

³¹⁴ Time Projection Chamber (TPC), out of a maximum of 159. The Particle IDentification
³¹⁵ (PID) criteria for all decay daughters are based on the requirement that the specific energy
³¹⁶ loss (dE/dx) is measured in the TPC within three standard deviations (σ_{TPC}) from the
expected value (dE/dx_{exp}), computed using a Bethe-Bloch parametrization [5].

Common track selections	$ \eta_{\text{lab}} $	< 0.8
	p_T	$> 0.15 \text{ GeV}/c$
	PID $ (\text{d}E/\text{d}x) - (\text{d}E/\text{d}x)_{\text{exp}} $	$< 3 \sigma_{\text{TPC}}$
Primary track selections	DCA _{<i>z</i>} to PV	$< 2 \text{ cm}$
	DCA _{<i>r</i>} to PV	$< 7\sigma_r - 10\sigma_r (p_T)$
	number of SPD points	≥ 1
	number of TPC points	> 70
	χ^2 per cluster	< 4

Table 5: Track selections common to all decay daughters and primary track selections applied to the charged pions from decays of Ξ^{*0} .

³¹⁷ Since pions and protons from weak decay of Λ ($c\tau = 7.89 \text{ cm}$ [10]) and pions from weak
³¹⁸ decay of Ξ^- ($c\tau = 4.91 \text{ cm}$ [10]) are produced away from the PV, specific topological and
³¹⁹ track selection criteria, as summarized in Table 6, were applied [11, 9, 12].

Topological cuts	p–Pb	Pb–Pb
DCA _{<i>r</i>} of Λ decay products to PV	$> 0.06 \text{ cm}$	$> 0.11 \text{ cm}$
DCA between Λ decay products	$< 1.4 \text{ cm}$	$< 0.95 \text{ cm}$
DCA of Λ to PV	$> 0.015 \text{ cm}$	> 0.06
$\cos\theta_\Lambda$	> 0.875	> 0.998
$r(\Lambda)$	$0.2 < r(\Lambda) < 100 \text{ cm}$	$0.2 < r(\Lambda) < 100 \text{ cm}$
$ M_{p\pi} - m_\Lambda $	$< 7 \text{ MeV}/c^2$	$< 7 \text{ MeV}/c^2$
DCA _{<i>r</i>} of pion (from Ξ^-) to PV	$> 0.015 \text{ cm}$	$> 0.035 \text{ cm}$
DCA between Ξ^- decay products	$< 1.9 \text{ cm}$	< 0.275
$\cos\theta_\Xi$	> 0.981	> 0.9992
$r(\Xi^-)$	$0.2 < r(\Xi^-) < 100 \text{ cm}$	$0.2 < r(\Xi^-) < 100 \text{ cm}$
$ M_{\Lambda\pi} - m_\Xi $	$< 7 \text{ MeV}/c^2$	$< 7 \text{ MeV}/c^2$

Table 6: Topological and track selection criteria.

³²¹ In the analysis of Ξ^{*0} , Λ and π from Ξ^- were selected with a DCA of less than 1.9 cm
³²² and with a DCA_{*r*} to the PV greater than 0.015 cm. The Λ daughter particles (π and p)
³²³ were required to have a DCA_{*r*} to the PV greater than 0.06 cm, while the DCA between the
³²⁴ two particles was required to be less than 1.4 cm. Cuts on the invariant mass, the cosine

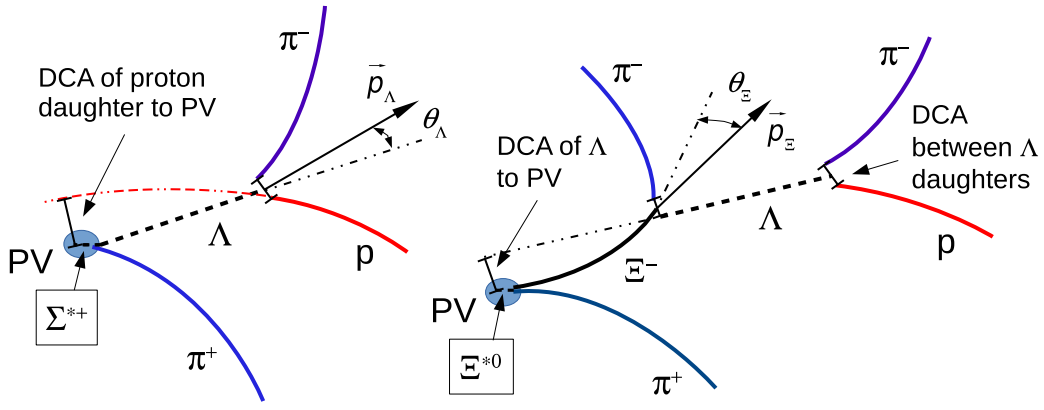


Figure 6: Sketch of the decay modes for Ξ^{*0} (right) and depiction of the track and topological selection criteria.

³²⁵ of the pointing angle ($\theta_\Lambda, \theta_\Xi$) and the radius of the fiducial volume ($r(\Lambda), r(\Xi)$) in Table 6
³²⁶ were applied to optimize the balance of purity and efficiency of each particle sample.

327 **5.1.3 Particle identification**

328 PID selection criteria are applied for

- 329 1. π^\pm (last emitted π) and proton from Λ
330 2. π^\pm (second emitted π) from Ξ^\pm
331 3. π^\pm (first emitted π) from $\Xi(1530)^0$

332 by using TPC. On TPC dE/dx versus momentum distribution, 3σ cuts are applied to TPC
333 for selecting each of the particles. The TPC dE/dx selection allows to have better signal
334 with $\sim 20\%$ increase of significance.

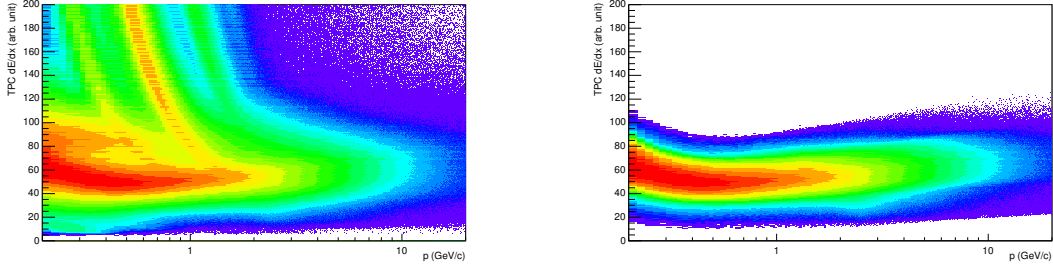


Figure 7: TPC dE/dx as function of transverse momentum for total (top) and selected first emitted π in 3σ (bottom)

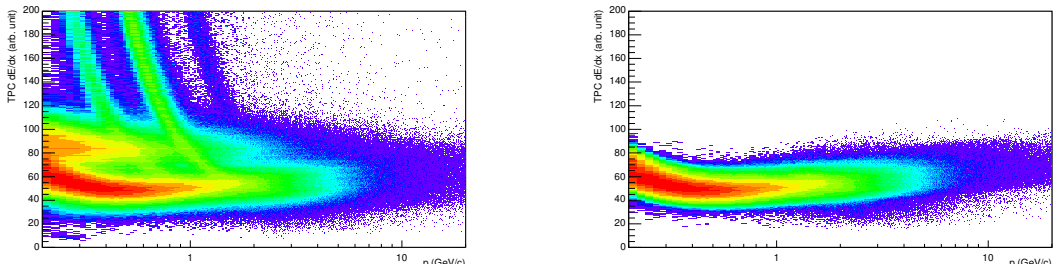


Figure 8: TPC dE/dx as function of transverse momentum for total (top) and selected second emitted π in 3σ (bottom)

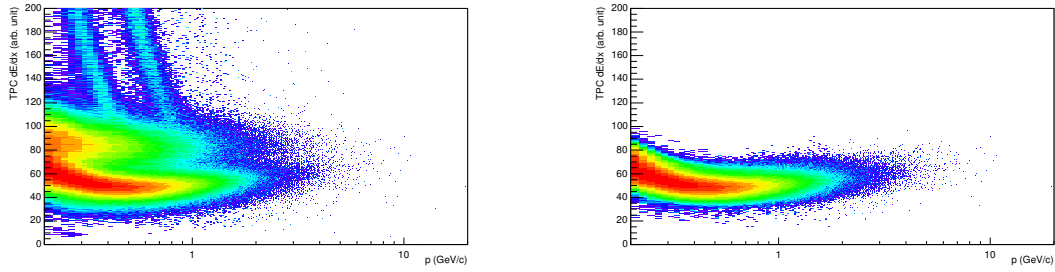


Figure 9: TPC dE/dx as function of transverse momentum for total (top) and selected last emitted π in 3σ (bottom)

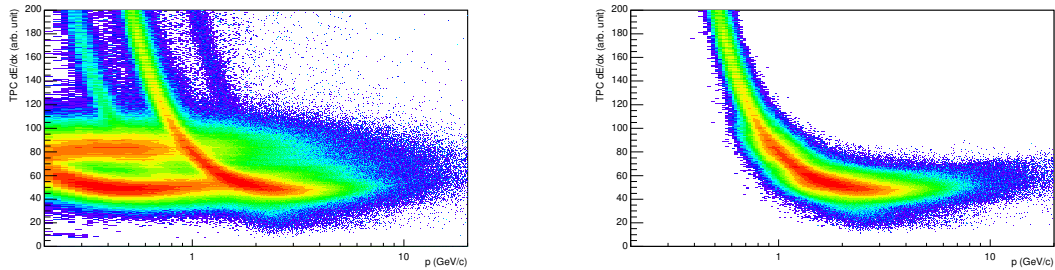


Figure 10: TPC dE/dx as function of transverse momentum for total (top) and selected proton in 3σ (bottom)

335 **5.1.4 Signal extraction**

336 The Ξ^{*0} signals were reconstructed by invariant-mass analysis of candidates for the decay
 337 products in each transverse momentum interval of the resonance particle, and for each
 338 multiplicity class. The $\Xi^-\pi^+(\Xi^+\pi^-)$ invariant mass distribution is reported in Figure 5.1.4
 339 for semi-central events (20-40%) in p–Pb collisions and Figure 5.1.4 for central events(0-
 340 10%) in Pb–Pb collisions.

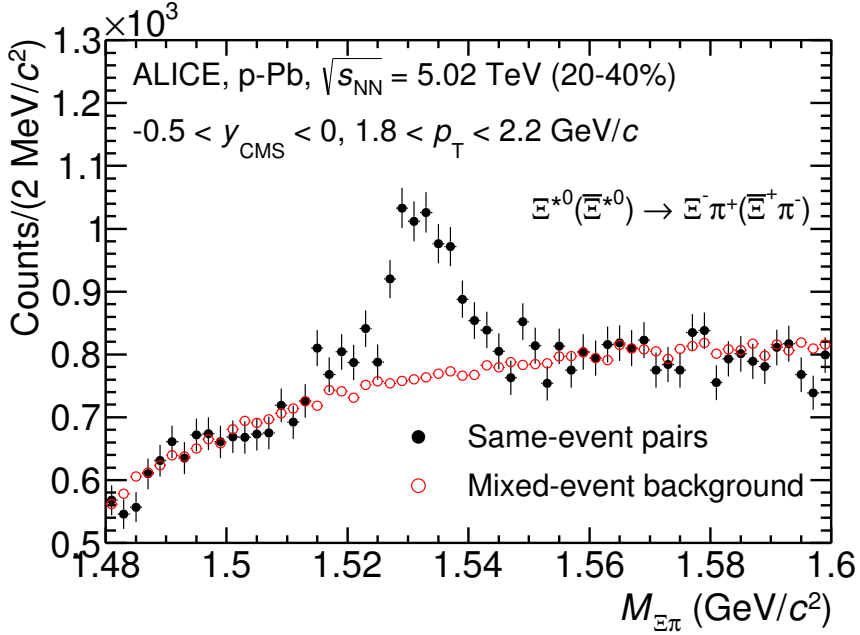


Figure 11: The $\Xi^\pm\pi^\pm$ invariant mass distribution (Same-event pairs) in $1.8 < p_T < 2.2$ GeV/c and for the multiplicity class 20-40%. The background shape, using pairs from different events (Mixed-event background), is normalised to the counts in $1.49 < M_{\Xi\pi} < 1.51$ GeV/c² and $1.56 < M_{\Xi\pi} < 1.58$ GeV/c².

341 Since the resonance decay products originate from a position which is indistinguishable
 342 from the PV, a significant combinatorial background is present. In order to extract
 343 $\Xi(1530)^0$ signal it is necessary to remove or, at least reduce, the combinatorial background.
 344 For this analysis, this has been done with the event mixing (EM) technique, by combining
 345 uncorrelated decay products 20 different events in p–Pb (5 different events in Pb–Pb). The
 346 events for the mixing have been selected by applying the similarity criteria to minimise
 347 distortions due to different acceptances and to ensure a similar event structure, only tracks
 348 from events with similar vertex positions z ($|\Delta z| < 1$ cm) and track multiplicities n ($|\Delta n| <$
 349 10) were taken.

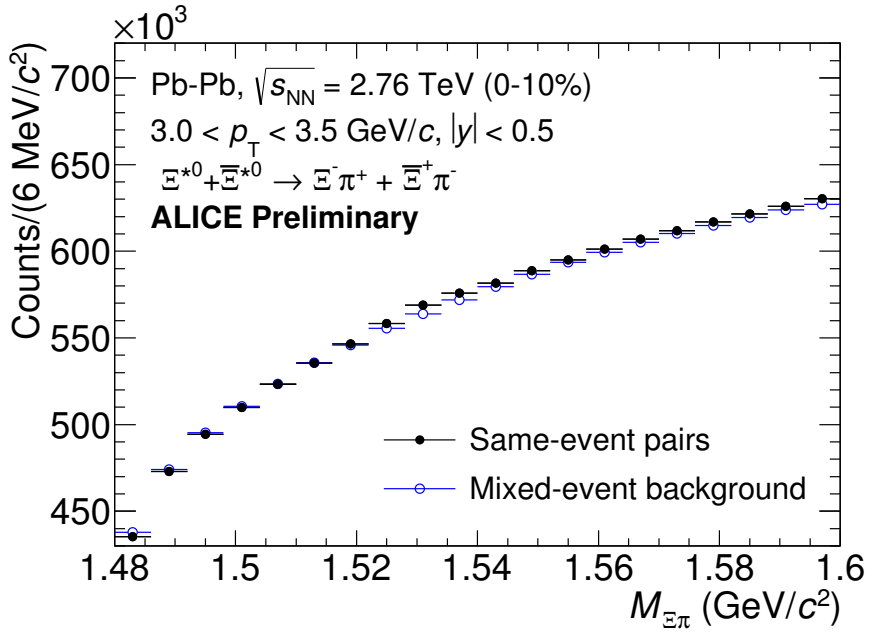


Figure 12: The $\Xi^\pm\pi^\pm$ invariant mass distribution (Same-event pairs) in $3.0 < p_T < 3.5$ GeV/c and for the centrality class 0-10%. The background shape, using pairs from different events (Mixed-event background), is normalised to the counts in $1.49 < M_{\Xi\pi} < 1.51$ GeV/c² and $1.56 < M_{\Xi\pi} < 1.58$ GeV/c².

350 The mixed-event background distributions were normalised to two fixed regions,
 351 $1.49 < M_{\Xi\pi} < 1.51 \text{ GeV}/c^2$ and $1.56 < M_{\Xi\pi} < 1.58 \text{ GeV}/c^2$, around the Ξ^{*0} mass
 352 peak (Figure 5.1.4 and 5.1.4). These regions were used for all p_T intervals and multiplicity
 353 classes, because the background shape is reasonably well reproduced in these regions and
 354 the invariant-mass resolution of the reconstructed peaks appears stable, independently of
 355 p_T . The uncertainty on the normalisation was estimated by varying the normalisation
 356 regions and is included in the quoted systematic uncertainty for the signal extraction (Sec-
 357 tion 5.4).

358 After the background subtraction, the resulting distribution is shown in Figure 5.1.4
 359 and 5.1.4. In order to obtain raw yields, a combined fit of a first-order polynomial for
 360 the residual background and a Voigtian function (a convolution of a Breit-Wigner and a
 361 Gaussian function accounting for the detector resolution) for the signal was used. The
 362 mathematical form of fit function used in analysis is:

$$f(M_{\Xi\pi}) = \frac{Y}{2\pi} \frac{\Gamma_0}{(M_{\Xi\pi} - M_0)^2 + \frac{\Gamma_0^2}{4}} \frac{e^{-(M_{\Xi\pi} - M_0)/2\sigma^2}}{\sigma\sqrt{2\pi}} + bg(M_{\Xi\pi}) \quad (1)$$

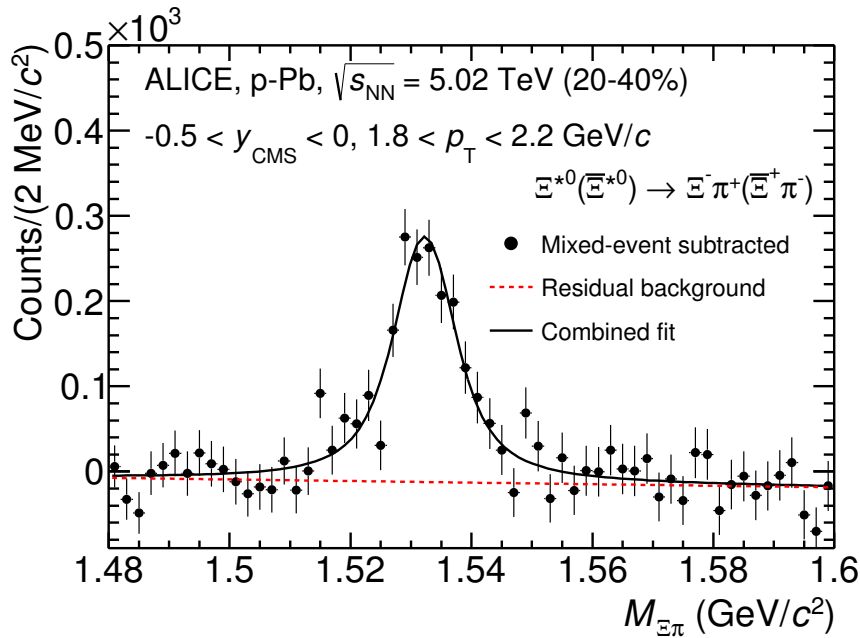


Figure 13: The invariant mass distribution after subtraction of the mixed-event background in p–Pb collisions. The solid curve represents the combined fit, while the dashed line describes the residual background.

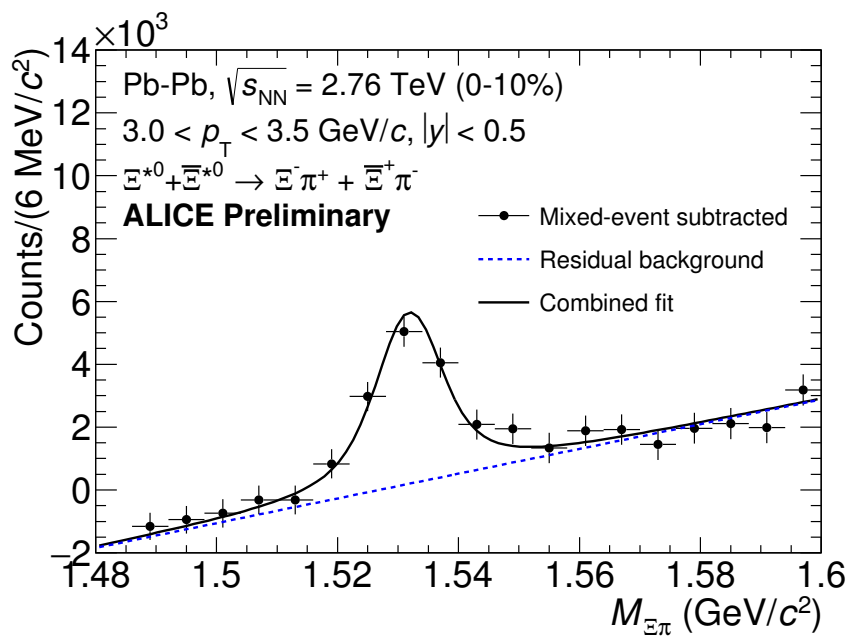


Figure 14: The invariant mass distribution after subtraction of the mixed-event background in Pb–Pb collisions. The solid curve represents the combined fit, while the dashed line describes the residual background.

363 The mass parameter of the Voigtian fit (M_0) is left free within the fit range ($1.48 \text{ GeV}/c^2$
364 and $1.59 \text{ GeV}/c^2$). The overall invariant mass width of the Voigtian function is governed
365 by 2 parameters: σ and Γ_0 . The σ describes the broadening of the peak due to finite
366 detector resolution while Γ describes the intrinsic width of the resonance itself. The Γ_0 is
367 fixed to the PDG value of $9.1 \text{ MeV}/c$ for the $\Xi(1530)^0$. Because of lack of statistics, the
368 σ can be over estimated. Therefore the σ parameter is fixed to value derived from σ in
369 MB events which has largest statistics. The σ as function of p_T distribution in MB events
370 is shown in Figure. 15 and we also report invariant mass of $\Xi(1530)^0$ as function of p_T in
371 Figure. 16. The $\Xi(1530)^0$ raw yields have been extracted from the fit for the 4 multiplicity
372 bins (+1NSD events) in p–Pb and 4 centrality bins in Pb–Pb collisions and the yields as
373 function of p_T are shown in Figure 17.

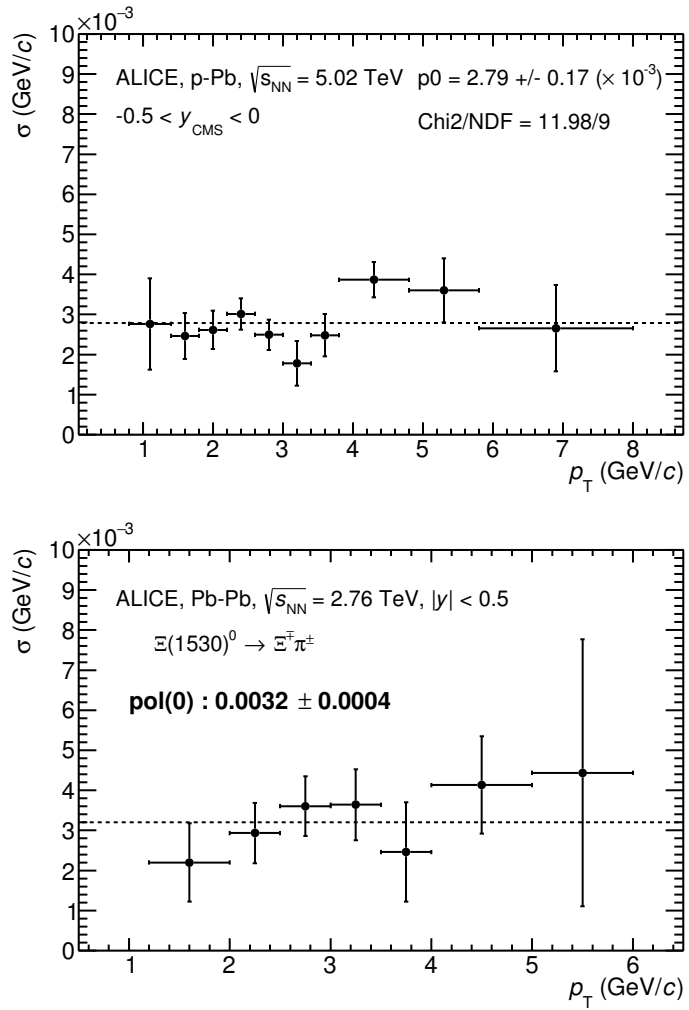


Figure 15: σ fit parameters as a function of p_T in MB in p–Pb collisions (top) and in Pb–Pb collisions (bottom).

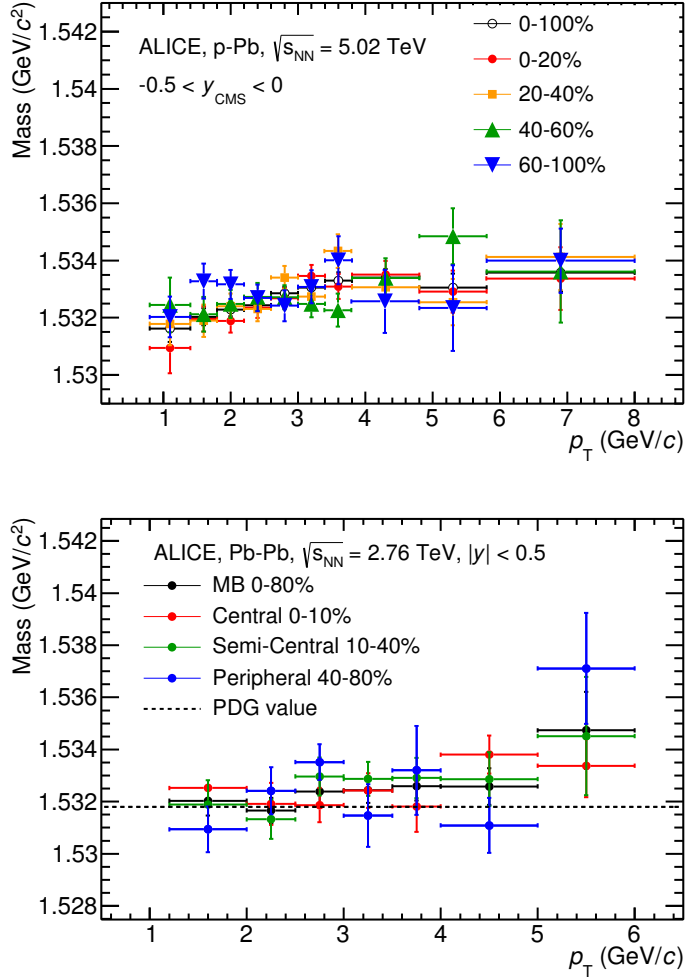


Figure 16: $\Xi(1530)^0$ -mass obtained from fit of the Voigtian peak as a function of p_T in each multiplicity classes in p-Pb collisions (top) and the different centrality classes in Pb-Pb (bottom).

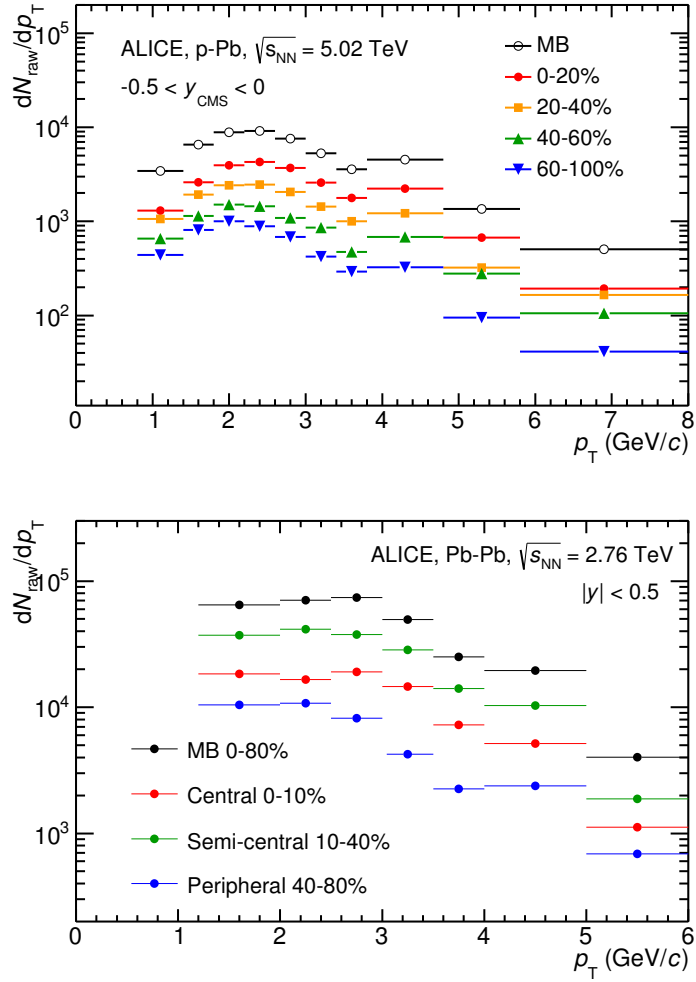


Figure 17: $\Xi(1530)^0$ -raw spectra obtained from fit of the Voigtian peak and a polynomial residual background for different multiplicities in p-Pb collisions (top) and Pb-Pb collisions (bottom). Only the statistical error is reported.

374 **5.2 Efficiency correction**

375 The raw yields were corrected for the geometrical acceptance and the reconstruction effi-
 376 ciency ($A \times \epsilon$) of the detector (Figure. 18). By using the DPMJET 3.05 event generator [13]
 377 and the GEANT 3.21 package [14], a sample of about 100 million p–Pb events was sim-
 378 ulated and reconstructed in order to compute the corrections. The distributions of $A \times \epsilon$
 379 were obtained from the ratio between the number of reconstructed Ξ^{*0} and the number of
 380 generated particle in the same p_T and rapidity interval. Since the correction factors for
 381 different multiplicity classes are in agreement with those from MB events within statistical
 382 uncertainty, the latter were used for all multiplicity classes.

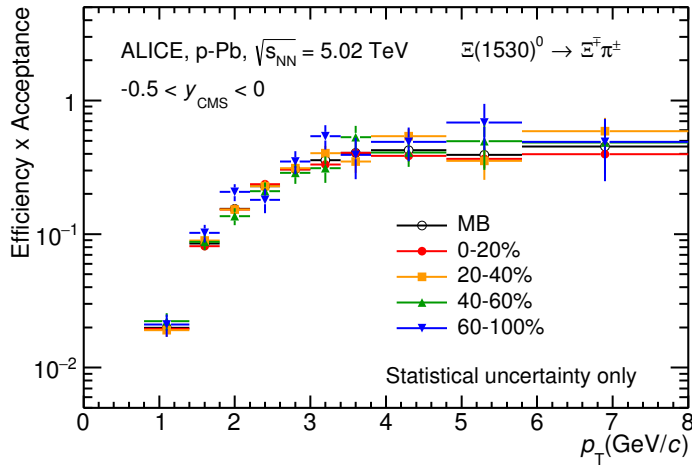


Figure 18: $\Xi(1530)^0$ -raw spectra obtained from fit of the Voigtian peak and a polynomial residual background for different multiplicities. Only the statistical error is reported.

383 Because the generated $\Xi(1530)^0$ spectra have different shapes than the measured $\Xi(1530)^0$
 384 spectra, it is necessary to weight the generated and reconstructed $\Xi(1530)^0$ spectra in these
 385 simulations. Fig. 19 shows the generated and reconstructed $\Xi(1530)^0$ spectra plotted with
 386 the (corrected) measured $\Xi(1530)^0$ spectrum for MB events and the Levy fit of that mea-
 387 sured spectrum. The generated and measured $\Xi(1530)^0$ spectra have different behaviours
 388 for the range $0.5 < p_T < 1$ GeV/ c . The generated $\Xi(1530)^0$ spectrum decreases with
 389 increasing p_T over this range, while the fit of the measured $\Xi(1530)^0$ spectrum reaches a
 390 local maximum in this range. The correction ϵ is observed to change rapidly over this
 391 p_T range. It is therefore necessary to weight the generated spectrum so that it has the
 392 shape of the measured $\Xi(1530)^0$ spectrum (and to apply corresponding weights to the re-
 393 constructed $\Xi(1530)^0$ spectrum). An iterative procedure is performed to determine the
 394 correct weighting (and therefore the correct ϵ).

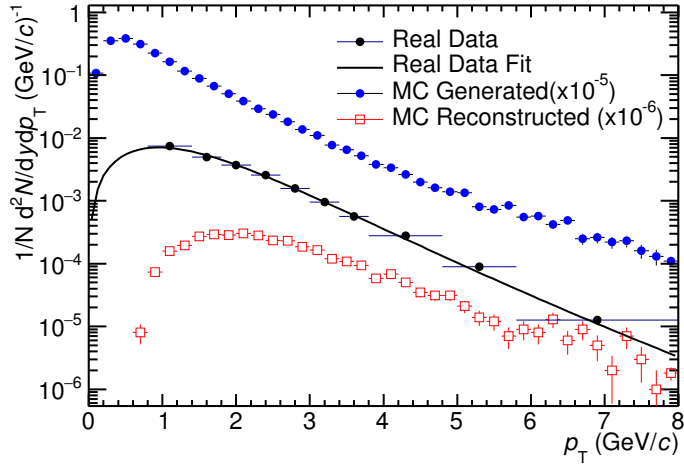


Figure 19: Real corrected $\Xi(1530)^0$ spectrum (black) for the minimum bias with Levy fit (black curve). Also shown are the unweighted generated (blue) and reconstructed (red) $\Xi(1530)^0$ spectra.

- 395 1. The unweighted ϵ is calculated.
- 396 2. This ϵ is used to correct the measured xis spectrum.
- 397 3. The corrected $\Xi(1530)^0$ spectrum is fit.
- 398 4. This fit is used to weight the simulated xis spectra. A p_T dependent weight is applied
399 to the generated xis spectrum so that it follows the fit. The same weight is applied
400 to the reconstructed xis spectrum.
- 401 5. The (weighted) ϵ is calculated.
- 402 6. Steps 2-5 are repeated (with the weighted ϵ from step 5 used as the input for step 2)
403 until the ϵ values are observed to change by $< 0.1\%$ (relative) between iterations. It
404 is observed that four iterations are sufficient for this procedure to converge.

405 Finally, the re-weighted efficiency is obtained and the distribution as function of p_T is
406 shown in Figure 20.

407 In order to obtain the correction factor dedicated in Pb-Pb collisions, MC events are
408 generated using Heavy Ion Jet Interaction Generator (HIJING). The generated events are
409 passed through a GEANT3 model of the ALICE experiment with a realistic description of
410 the detector response. Because we have observed centrality dependent efficiency, the cen-
411 trality dependent efficiencies have been applied to get corrected raw yield. The reweighting

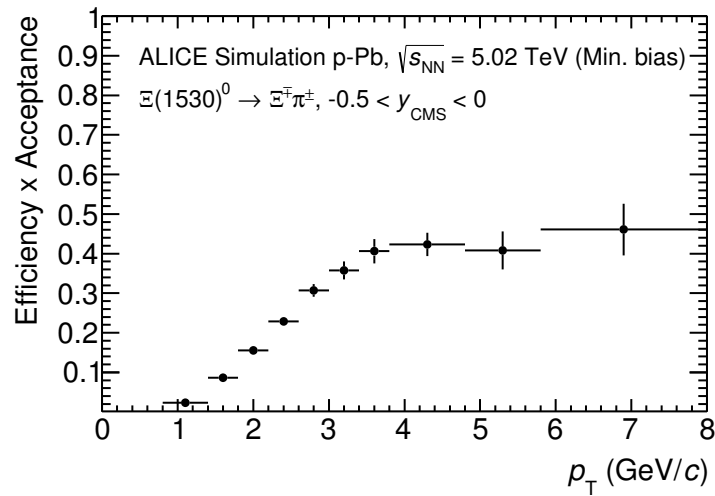


Figure 20: Efficiency as a function of p_T in minimum bias events in p–Pb collisions.

⁴¹² approach which was used to correct the efficiency in p–Pb is also applied to the efficiency
⁴¹³ obtained in Pb–Pb.

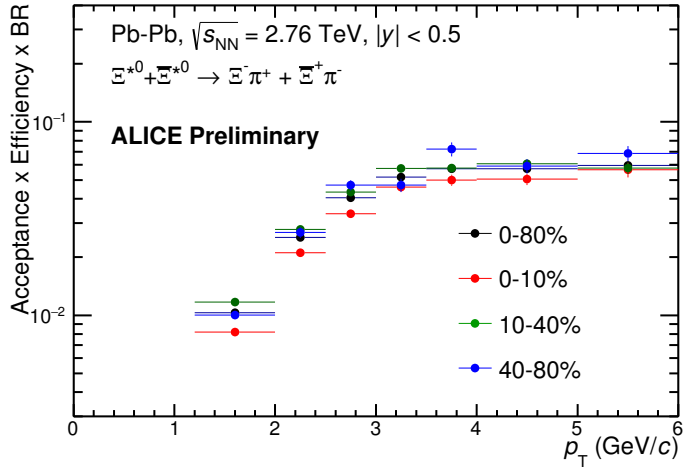


Figure 21: Efficiency as a function of p_T in different centrality classes in Pb–Pb collisions

414 5.3 Corrected p_T -spectra

415 The p_T spectrum is by the number of produced particles of a given type in the desired
 416 interval of phase-space divided by the number of inelastic collisions. The spectrum is
 417 calculated as:

$$\frac{1}{N} \times \frac{d^2N}{dydp_T} = \frac{1}{N_{E,PhysSel}} \times \frac{N_{raw}}{dp_T dy} \frac{1}{\epsilon} \frac{N_{total}^{MC}}{N_{post-PVcut}^{MC}}, \quad (2)$$

418 where N_E represent the number inelastic collisions, the $\frac{dN}{dydp_T}$ is the yield per range of
 419 rapidity y , per range in p_T . On the right hand side $N_{E,PhysSel}$ is the number of events
 420 counted by the physics selection trigger. N_{raw} is the raw extracted number of particle in the
 421 rapidity and p_T bin of width $\Delta y = 0.5$ in p–Pb ($\Delta y = 1.0$ in Pb–Pb) and Δp_T , respectively.
 422 ϵ is the reconstruction efficiency estimated from Monte Carlo simulations. $\frac{N_{total}^{MC}}{N_{post-PVcut}^{MC}}$ is the
 423 ratio of the total number of particle from MC divided by the number of particle from MC
 424 after the Primary-Vertex cut is imposed. It takes into account the fraction of particle lost
 425 after imposing the PV cut. We notice that for minimum-bias results in p–Pb, we adopted
 426 a normalisation such that to provide result from non-single diffractive(NSD) cross-section.
 427 The normalisation factor is 0.964 [6]. The obtained spectrum at MB and the spectrums
 428 from different multiplicity classes in p–Pb are shown in Figure 22 and different centrality
 429 classes in Pb–Pb are shown in Figure 23.

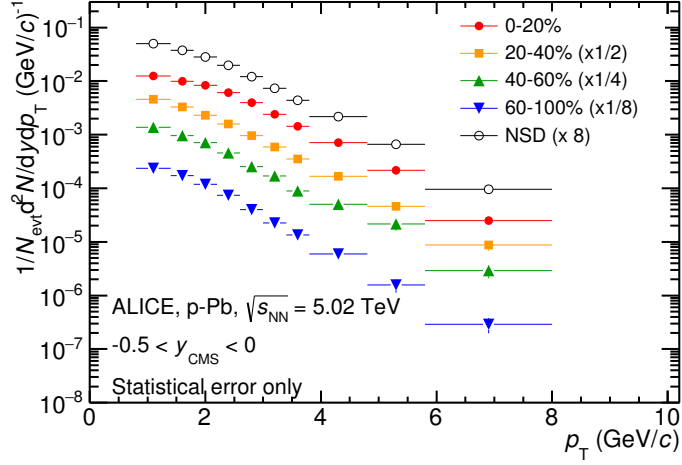


Figure 22: Corrected p_T -spectra of $\Xi(1530)^0$ in NSD and different multiplicity classes in p–Pb collisions.

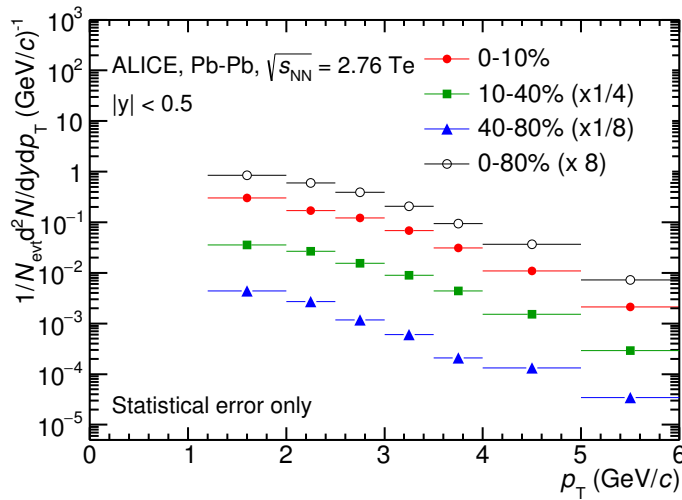


Figure 23: Corrected p_T -spectra of $\Xi(1530)^0$ in different centrality classes in Pb-Pb collisions.

430 **5.4 Systematic uncertainties**

431 The systematic uncertainties are calculated in seven principle groups. The procedure to ob-
 432 tain the systematic uncertainties is performed many times by varying the possible permuta-
 433 tion of the analysis parameter. The general strategy for evaluating systematic uncertainties
 434 is described as following:

- 435 1. Choose one set of parameters for the analysis as default
- 436 2. Observe the deviation of yield when one parameter is changed
- 437 3. The systematic uncertainty is calculated for a given source as the RMS deviation of
 438 the available sources.
- 439 4. The total systematic uncertainty, taking into account all the different sources, is the
 440 sum in quadrature of each source.

441 To study the systematic effect we repeat the measurement by varying one parameter at
 442 a time. A Barlow [15] check has been performed for each measurement to verify whether it
 443 is due to a systematic effect or a statistical fluctuation. Let each measurement be indicated
 444 by $(y_i \pm \sigma_i)$ and the central value (default measurement) by $(y_c \pm \sigma_c)$, one can define $\Delta\sigma_i$
 445 (Eq. 3).

$$\Delta\sigma_i = \sqrt{(\sigma_i^2 - \sigma_c^2)} \quad (3)$$

446 Then we calculate $n_i = \Delta y_i / \Delta\sigma_i$, where $\Delta y_i = |y_c - y_i|$. If $n_i \leq 1.0$ then the effects
 447 are due to the statistical fluctuation and if $n_i > 1.0$ we apply consistency check. Since
 448 the alternate and default measurements are not statistically independent, an alternate
 449 measurement which is statistically consistent with the default measurement should not be
 450 used in calculating a systematic uncertainty. The difference between the two measurements
 451 is $\Delta = y_c - y_i$. The difference in quadrature of the uncertainties is calculated by Eq. 3. It
 452 could be possible to check if $\Delta < \sigma$ and exclude such cases from the systematic uncertainties.
 453 However, there can be statistical fluctuations for which $\Delta > \sigma$. If the variations between the
 454 default and alternate measurements are purely statistical, the distribution of Δ/σ should
 455 be a Gaussian with a mean value that is consistent with zero and a deviation σ consistent
 456 with unity. In this analysis, if the mean value is less than 0.1 and σ is less than 1, the
 457 variation passes the consistency check.

458 Only the measurements which passed the Barlow check ($n_i > 1$) are used to determine
 459 the systematic uncertainty. For measurements $N > 2$, the systematic uncertainty has been
 460 determined as the RMS (eqn. 4) of the available measurements. If $N=2$, the absolute
 461 difference is assigned as systematic uncertainty.

$$\delta y_{syst.} = \sqrt{\frac{1}{N} \sum_i (y_i - \bar{y})^2} \quad (4)$$

462 Here N is the total number of available measurements including y_c and \bar{y} is the average
463 of value of the measurements. The measurement did not pass Barlow check, zero systematic
464 uncertainty has been assigned to the value.

465 By suing the way as explained above, all the main contributions to the systematic un-
466 certainty of particle spectra have been studied. In particular those that comes from signal
467 extraction, topological and kinematical selection cuts, track quality selection and $n\sigma$ TPC
468 PID variation. the meaning of each source of systematic uncertainty studied is described
469 in the following:

470

471 **Signal extraction**

472 We have extracted the signal with varying the yield calculating method which contains
473 the method of signal extraction by integrating the Voigtian fit function and bin counting.
474 We also have varied the normalisation range which is related to the invariant mass region
475 where the mixed events distribution is scaled to subtract the combinatorial background
476 and different background estimator such as Like-Sign distribution and polynomial fit was
477 taken account into the systematic source of signal extraction. The systematic uncertainty
478 from signal extraction is sum in quadrature of three sources.

479

480 **Topological selection**

481 To evaluate the stability of the chosen set of values for the topological cuts, loose and tight
482 cuts have beed defined in order to vary by $\pm 10\%$ respectively. The parameters are changed
483 once at a time. Total systematic uncertainty from topological selection is calculated by
484 summation in quadrature of nine sources.

485

486 **TPC $N_{cluster}$ selection**

487 The selection performed for the daughter tracks of the cascade is that $N_{cluster}$ is larger
488 than 70 and the value has been varied to 60 and 80 in order to estimate the systematic
489 uncertainty due to this selection.

490

491 **TPC dE/dx selection**

492 In order to evaluate any potential effect due to the TPC dE/dx selection (U_{PID}), the N_σ
493 selection was varied with $N = 2.5$ and 3.5 .

494

495 **p_T shape correction**

496 As described in Section 5.2, due to the different shape of the measured and generated
497 $\Xi(1530)^0$ spectra, we have applied reweighing procedure to the generated spectra to have
498 same shape and this correction is added into contributor of systematic uncertainty as
499 p_T shape correction.

500

501 **Mass window range selection**

502 In order to select Ξ^\pm which is daughter particle of $\Xi(1530)^0$, we apply the mass window

503 ± 7 MeV/ c^2 around $\Xi(1530)^0$ mass on $\Lambda\pi$ invariant mass distribution. The boundaries
504 has been varied to ± 6 MeV/ c^2 and ± 8 MeV/ c^2 to estimate systematic uncertainty.

505

506 **Vertex range selection**

507 The distribution of vertex-z is shown in Fig.3. The cut on |Vz| was varied from the nominal
508 ± 10 cm to ± 9 cm, ± 11 cm.

509

510 **Material Budget and hadronic cross section**

511 A possible source of uncertainty comes from the description of the material, active (de-
512 tecting area) or dead (structure and cable), that the particles cross during their travel in
513 the MC with respect to the real material present in the detector. Such description could
514 affect the reconstruction efficiency in different aspects (e.g. multiple scattering, energy
515 loss). The value estimated by Ξ analysis [16] has been used in this study which gives 4%
516 systematic uncertainty. In case of systematic uncertainty from hadronic cross section, we
517 have inherited the value studied in previous measurement[17] which amount is 1%.

518

519 **Tracking efficiency**

520 Systematic uncertainties from tracking efficiency from ITS + TPC combined track were
521 assigned as 3% in p–Pb and 4% in Pb–Pb collision system.[17]
522 (<https://twiki.cern.ch/twiki/bin/view/ALICE/TrackingEfficiencyCharged>)

523

524 Finally, total systematic uncertainty is sum in quadrature of sources listed above. Fig-
525 ure 24 and Figure 25 show the total systematic uncertainty in minimum bias event and
526 different multiplicity classes in p–Pb collisions, respectively. Again, Figure 26 and Figure
527 27 present the total systematic uncertainty in minimum bias event and different centrality
528 classes in Pb–Pb collisions.

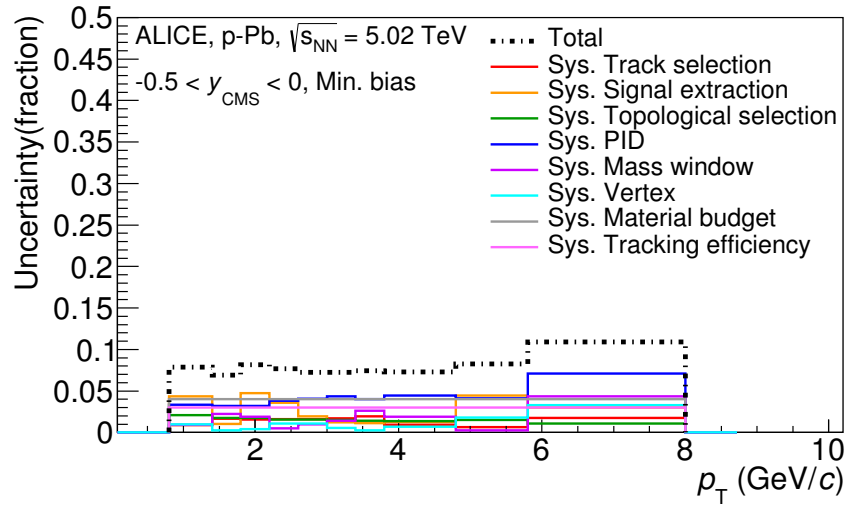


Figure 24: Summary of the contributions to the systematic uncertainty in minimum bias events in p–Pb collisions. The dashed black line is the sum in quadrature of all the contributions.

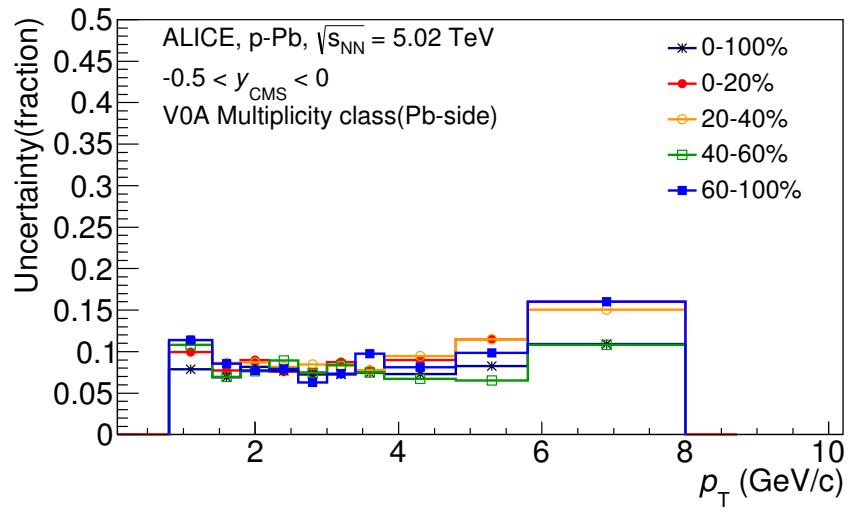


Figure 25: Systematic uncertainties for each multiplicity classes in p–Pb collisions.

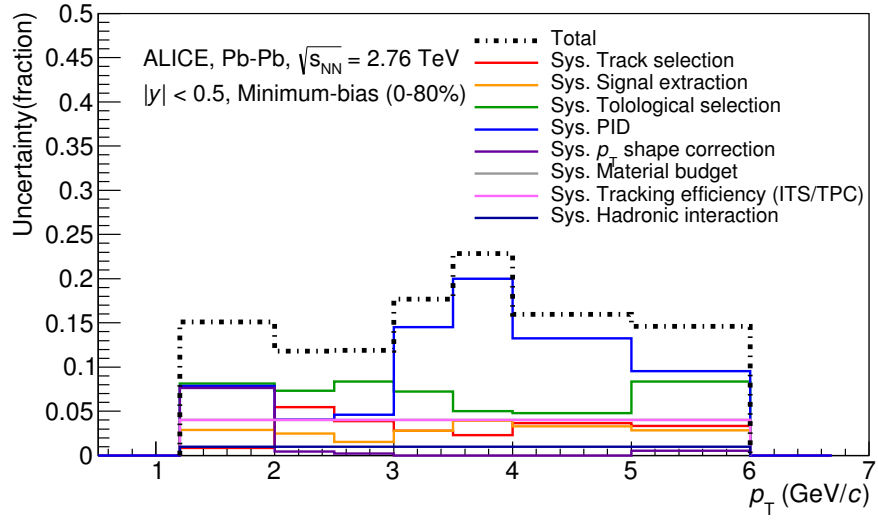


Figure 26: Summary of the contributions to the systematic uncertainty in minimum bias events in Pb–Pb collisions. The dashed black line is the sum in quadrature of all the contributions.

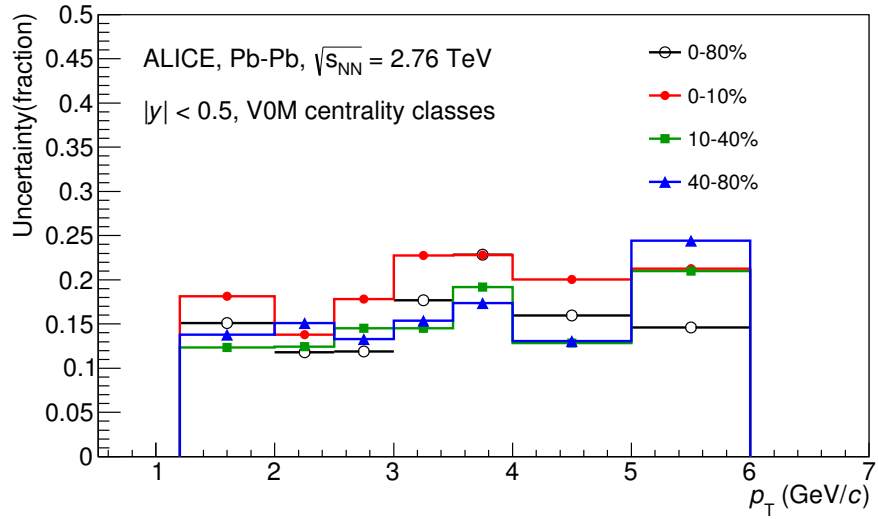


Figure 27: Systematic uncertainties for each multiplicity classes.

Source of uncertainty	$\Xi(1530)^0$ in p-Pb	$\Xi(1530)^0$ in Pb-Pb
<i>p_T-dependent</i>		
Tracking efficiency	3%	4%
Tracks selection	1-2%	1-5%
Topological selection	1-2%	5-8%
PID	3-7%	4-20%
Signal extraction	1-5%	1-4%
<i>p_T</i> shape correction	-	0-8%
Mass window (Ξ^{\pm})	4	-
Vertex selection	3%	-
<i>p_T-independent</i>		
Hadronic interaction	-	1%
Material budget	4%	4%
Branching ratio	0.3%	0.3%
Total	8-12%	9-25 %

Table 7: Summary of the systematic uncertainties on the differential yield, $d^2N/(dp_T dy)$. Minimum and maximum values in all p_T intervals and multiplicity classes in p–Pb, centrality classes in Pb–Pb are shown for each source.

529 5.5 $\Xi(1530)^0$ transverse momentum spectra

530 The raw yield shown in Figure 22 and 23 have been corrected for efficiency as described
 531 in section 5.2. The measured spectra for $(\Xi(1530)^0 + \bar{\Xi}(1530)^0)/2$ are reported in Figure
 532 28 for p–Pb collisions and Figure 29 for Pb–Pb collisions. The statistical and systematic
 533 uncertainties are reported respectively as the error bars and the boxes on the plot. The
 534 corrected yields for p–Pb collisions are measured with $0.8 < p_T < 8.0$ GeV/c while the
 535 yields for Pb–Pb collisions are obtained with $1.2 < p_T < 6.0$ GeV/c due to difficulty of
 536 signal extraction in low and high p_T region.

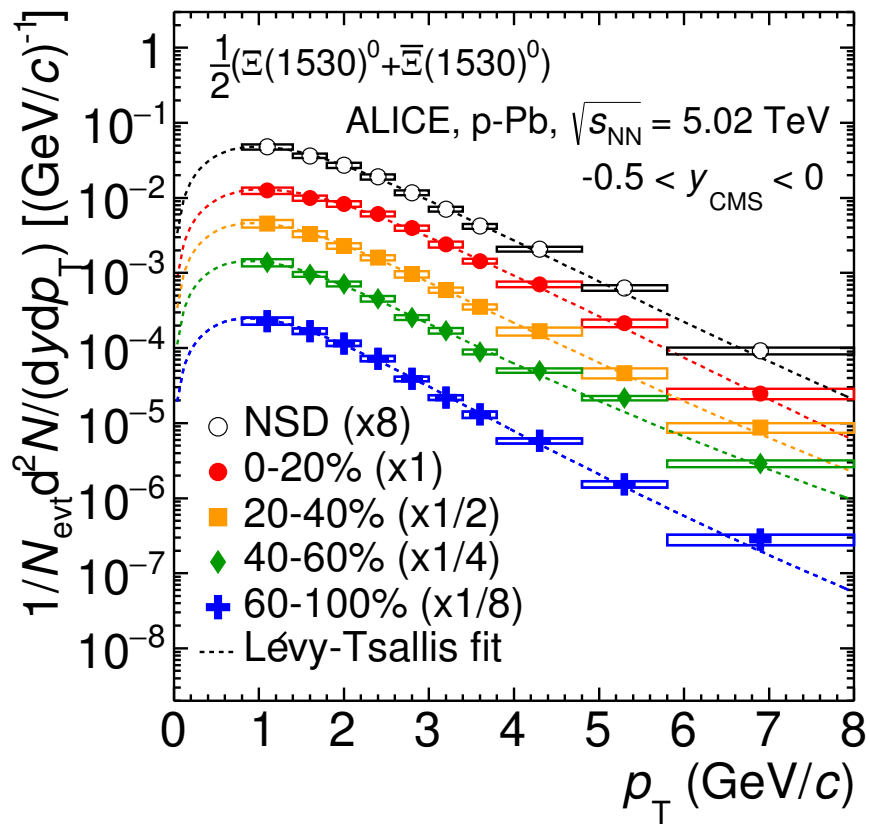


Figure 28: Corrected yields as function of p_T in NSD events and multiplicity dependent event classes in p-Pb collision system. Statistical uncertainties are presented as bar and systematical uncertainties are plotted as boxes.

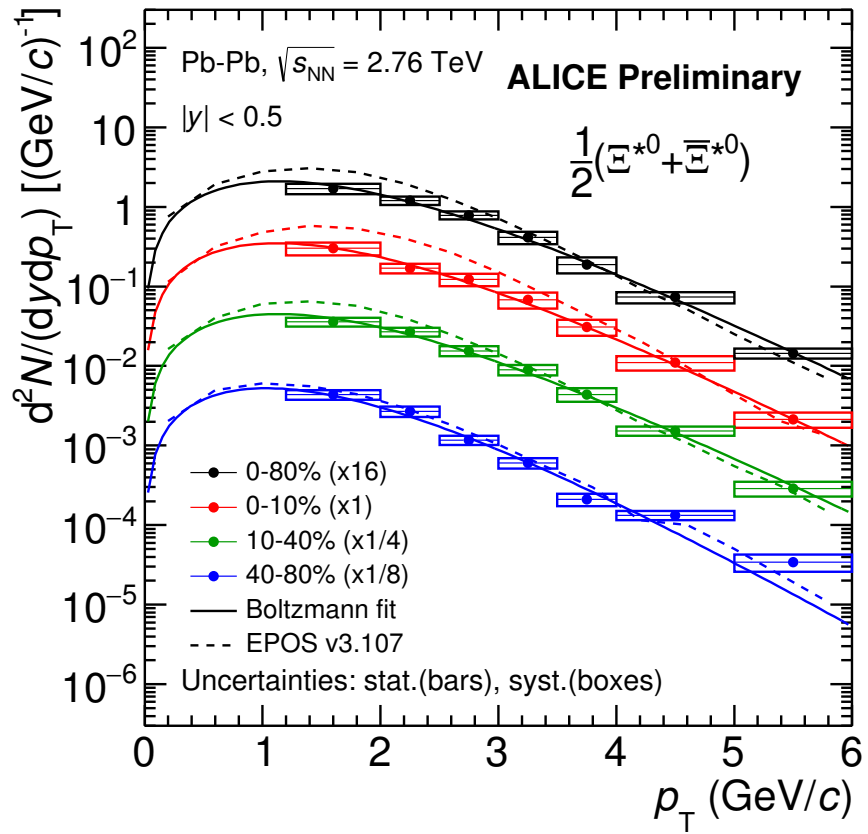


Figure 29: Corrected yields as function of p_T in different centrality classes in Pb-Pb collision system. Statistical uncertainties are presented as bar and systematical uncertainties are plotted as boxes.

537 **6 Results**

538 **6.1 dN/dy and $\langle p_T \rangle$**

539 **6.2 Particle yield ratios**

540 **6.2.1 Comparison with other resonances**

541 **6.2.2 Comparison with models**

542 **References**

- 543 [1] D. Hahn and H. Stoecker, “THE QUANTUM STATISTICAL MODEL OF
544 FRAGMENT FORMATION: ENTROPY AND TEMPERATURE EXTRACTION
545 IN HEAVY ION COLLISIONS,” *Nucl. Phys.* **A476** (1988) 718–772.
- 546 [2] S. Wheaton, J. Cleymans, and M. Hauer, “THERMUS: A Thermal model package
547 for ROOT,” *Comput. Phys. Commun.* **180** (2009) 84–106, [hep-ph/0407174](#).
- 548 [3] J. Cleymans, S. Kabana, I. Kraus, H. Oeschler, K. Redlich, and N. Sharma,
549 “Antimatter production in proton-proton and heavy-ion collisions at ultrarelativistic
550 energies,” *Phys. Rev.* **C84** (2011) 054916, [arXiv:1105.3719 \[hep-ph\]](#).
- 551 [4] **ALICE** Collaboration, K. Aamodt *et al.*, “The ALICE experiment at the CERN
552 LHC,” *JINST* **3** (2008) S08002.
- 553 [5] **ALICE** Collaboration, B. Abelev *et al.*, “Performance of the ALICE Experiment at
554 the CERN LHC,” *Int. J. Mod. Phys.* **A29** (2014) 1430044, [arXiv:1402.4476](#)
555 [[nucl-ex](#)].
- 556 [6] **ALICE** Collaboration, J. Adam *et al.*, “Production of $K^*(892)^0$ and $\phi(1020)$ in
557 $p\text{-Pb}$ collisions at $\sqrt{s_{NN}} = 5.02$ TeV,” *Eur. Phys. J.* **C76** (2016) 245,
558 [arXiv:1601.7868 \[nucl-ex\]](#).
- 559 [7] **ALICE** Collaboration, B. Abelev *et al.*, “Pseudorapidity Density of Charged
560 Particles in $p\text{-Pb}$ Collisions at $\sqrt{s_{NN}} = 5.02$ TeV,” *Phys. Rev. Lett.* **110** (2013)
561 032301, [arXiv:1210.3615 \[nucl-ex\]](#).
- 562 [8] **ALICE** Collaboration, B. Abelev *et al.*, “Centrality determination of Pb-Pb
563 collisions at $\sqrt{s_{NN}} = 2.76$ TeV with ALICE,” *Phys. Rev.* **C88** (2013) ,
564 [arXiv:1303.0737 \[nucl-ex\]](#).
- 565 [9] **ALICE** Collaboration, B. Abelev *et al.*, “Production of $\Sigma(1385)^{\pm}$ and $\Xi(1530)^0$ in
566 proton-proton collisions at $\sqrt{s} = 7$ TeV,” *Eur. Phys. J.* **C75** (2015) 1,
567 [arXiv:1406.3206 \[nucl-ex\]](#).

- 568 [10] **Particle Data Group** Collaboration, K. Olive *et al.*, “Review of Particle Physics,”
 569 *Chin. Phys. C***38** (2014) 090001.
- 570 [11] **ALICE** Collaboration, J. Adam *et al.*, “Multi-strange baryon production in p–Pb
 571 collisions at $\sqrt{s_{\text{NN}}}=5.02$ TeV,” *Phys. Lett. B***758** (2016) 389–401,
 572 [arXiv:1512.07227 \[nucl-ex\]](https://arxiv.org/abs/1512.07227).
- 573 [12] **ALICE** Collaboration, K. Aamodt *et al.*, “Strange particle production in
 574 proton-proton collisions at $\sqrt{s}=0.9$ TeV with ALICE at the LHC,” *Eur. Phys. J.*
 575 **C71** (2011) 1594, [arXiv:1012.3257 \[nucl-ex\]](https://arxiv.org/abs/1012.3257).
- 576 [13] S. Roesler, R. Engel, , and J. Ranft, “The Monte Carlo Event Generator
 577 DPMJET-III, Advanced Monte Carlo for Radiation Physics, Particle Transport
 578 Simulation and Applications,” *Conference Proceedings, MC2000, Lisbon, Portugal,*
 579 *October 23–26* (2000) 1033–1038, [hep-ph/0012252](https://arxiv.org/abs/hep-ph/0012252).
- 580 [14] R. Brun, F. Carminati, and S. Giani, “GEANT detector description and simulation
 581 tool,” *CERN-W5013* (1994) .
- 582 [15] R. Barlow, “Systematic Errors: Facts and Fictions,” *Presented at Advanced*
 583 *Statistical Techniques in HEP, Durham, March 2002* (2002) 333p,
 584 [hep-ex/0207026v1](https://arxiv.org/abs/hep-ex/0207026v1).
- 585 [16] **ALICE** Collaboration, B. Abelev *et al.*, “Multi-strange baryon production at
 586 mid-rapidity in Pb–Pb collisions at $\sqrt{s_{\text{NN}}}=2.76$ TeV,” *Phys. Lett. B***728** (2014)
 587 216–227, [arXiv:1307.5543 \[nucl-ex\]](https://arxiv.org/abs/1307.5543).
- 588 [17] **ALICE** Collaboration, B. Abelev *et al.*, “Centrality dependence of π , K and p
 589 production in Pb–Pb collisions at $\sqrt{s_{\text{NN}}}=2.76$ TeV,” *Phys. Rev. C***88** (2013) ,
 590 [arXiv:1301.4361 \[nucl-ex\]](https://arxiv.org/abs/1301.4361).

591 **Acknowledgements**